Assessing strength of phases in a quadruplex high entropy alloy via high-throughput nanoindentation to clarify origins of strain hardening

Jacob Weiss, Evgenii Vasilev, Marko Knezevic*

Department of Mechanical Engineering, University of New Hampshire, Durham, NH 03824, USA.

* Corresponding author at: University of New Hampshire, Department of Mechanical Engineering, 33 Academic Way, Kingsbury Hall, W119, Durham, New Hampshire 03824, United States. E-*mail address*: marko.knezevic@unh.edu (M. Knezevic).

Abstract

This paper describes the main findings from an experimental investigation into local and overall strength and fracture behavior of a microstructurally flexible, quadruplex, high entropy alloy (HEA), $Fe_{42}Mn_{28}Co_{10}Cr_{15}Si_5$ (in at%). The alloy consists of metastable face-centered cubic austenite (γ), stable hexagonal epsilon martensite (ε), stable body-centered cubic ferrite (α), and stable tetragonal sigma (σ) phases. The overall behavior of the alloy in compression features a great deal of plasticity and strain hardening before fracture. While the contents of diffusion created α and σ phases remain constant during deformation, the fraction of ε increases at the expanse of γ due to the diffusionless strain induced $\gamma \rightarrow \varepsilon$ phase transformation. High-throughput nanoindentation mapping is used to assess the mechanical hardness of individual phases contributing to the plasticity and hardening of the alloy. Increasing the fraction of the dislocated ε phase during deformation due to the transformation is found to act as a secondary source of hardening because γ and ε exhibit similar hardness at a given strain level. While these two phases exhibit moderate hardening during plasticity, significant softening is observed in σ owing to the phase fragmentation. While the phase transformation mechanism facilitates accommodation of the plasticity, the primary source of strain hardening in the alloy is the refinement of the structure during the transformation inducing a dynamic Hall-Petch-type barrier effect. Results pertaining to the evolution of microstructure and local behavior of the alloy under compression are presented and discussed clarifying the origins of strain hardening. While good under compression, the alloy poorly behaves under tension. Fracture surfaces after tension feature brittle micromechanisms of fracture. Such behavior is attributed to the presence of the brittle σ phase.

Keywords: High entropy alloys; Phase transformations; Microstructures; Nanoindentation; Hardness maps

1. Introduction

A class of sophisticated metallic materials termed high entropy alloys (HEAs) are being developed to enhance the contrasting material properties of strength and ductility [1-4]. Beginning with equiatomic HEA like $Fe_{20}Mn_{20}Ni_{20}Co_{20}Cr_{20}$ which exhibits good strength, ductility, and fracture toughness, other variants of the Fe-Mn-Ni-Co-Cr systems like $Fe_{40}Mn_{27}Ni_{26}Co_{5}Cr_{2}$ (at. %) are being explored [5-9]. The chief advantage of HEAs is in their flexibility to tune microstructural features through adjusting their composition and processing. To this end, dual phase HEAs consisting of Fe-Mn-Co-Cr were developed. For example, an $Fe_{50}Mn_{30}Co_{10}Cr_{10}$ (at. %) system consists of a face-centered cubic (FCC) austenite (γ) phase, which is metastable. The phase undergoes strain-induced phase transformation into a dislocated hexagonal close-packed (HCP) epsilon-martensite phase (ε) while accommodating plastic strains [8, 10]. The mechanism is often referred to as the TRIP (transformation induced plasticity) since it accommodates plastic strains like dislocation slip. Because multi-phase, these HEAs offer flexibility to design volume fraction and distribution of phases to improve ductility and strength tradeoffs [5, 6, 8]. The distribution can be achieved by varying processing methodologies such as rolling, high pressure torsion, and friction stir processing [11-13]. Studies on increasing alloying elements such as Cr at the expense of Fe and Mn on γ phase in dual phase HEA have been reported in [14, 15]. Increasing the Cr content furthers the driving force of $\gamma \rightarrow \varepsilon$ transformation [11]. The present work is concerned with characterizing a $Fe_{42}Mn_{28}Co_{10}Cr_{15}Si_{5}$ (in at%) HEA designed to exhibit pronounced TRIP. The alloy has a quadruplex structure consisting of stable body-centered cubic ferrite (α) and stable tetragonal sigma (σ) phases in addition to metastable γ and stable ε. The particular focus of the work is to assess the strength of individual phases via high-throughput nanoindentation and attempt to clarify origins of strain hardening during plastic deformation of the alloy.

Nanoindentation is conceived as a technique to measure and understand the localized mechanical properties of metallic materials including HEAs [16-18]. To date, hardness mapping has been utilized to explore spatial variations in a variety of metal alloys [19, 20]. However, only a handful of such experiments along with some atomistic simulations have been performed on nanoindentation of HEAs [21]. Atomistic simulations of nanoindentation of HEAs are challenging due to compositional complexities [22]. Nevertheless, such simulations were successful in revealing the effects of localized chemical composition changes on the mechanical properties of complex multicomponent HEAs [23-25]. Nanoindentation studies revealed the effects of single crystal crystallographic orientations on nanoindentation response and underlying defect structures [26]. Moreover, studies into the effects of twin boundaries on nanoindentation response and underlying dislocation activity found that the twin boundaries inhibit dislocation penetration through the analysis of the plastic zone underneath the indentation [27]. Another study analyzed the influences of alloy composition, crystal structure, grain size, and twin boundary distance on the nanoimprinted properties of several HEAs [28].

While various aspects of the mechanical response of HEA alloys under deformation by nanoindentation were investigated in the pre-mentioned studies, the role of local hardness in individual phases on strain hardening of multi-phase HEAs was not rationalized. Localized hardness mapping is a relatively new experimental technique that has been underutilized in only a few studies involving HEAs [29-31]. We subject a complex $Fe_{42}Mn_{28}Co_{10}Cr_{15}Si_{5}$ (in at%) HEA to nanoindentation over relatively large areas at varying strain levels to understand its hardening behavior more holistically. An experimental investigation into tailoring the content of phases and grain structure for high strength of the alloy using rolling, friction stir processing, and compression was performed in our earlier study [11]. Hardness maps obtained over selected areas in the present study provide complementary insights into the mechanical properties of evolving HEA microstructural phases.

The evolution of microstructure was measured by optical microscopy, electron back scatter diffraction (EBSD), and neutron diffraction (NeD). The as-received material was a rolled plate having a quadruplex structure consisting of metastable γ, stable σ, stable ε, along with some stable α phases. The evolution of phase fractions and texture per phase was measured. Simple compression data was taken from [11], while simple tension testing of the alloy was performed in the present work. In addition to measuring the overall properties, localized hardness Young's modulus maps over increasing levels of strain are measured. To this end, instrumented indentation testing (IIT) with the KLA Nano Indenter® systems employing the Oliver-Pharr method is used to automatically determine the sought properties from the recorded load-displacement history throughout the experiment [32]. These maps are correlated with the EBSD maps over the same areas, given that the resolution, scan size, and sample preparation requirements between the nanoindentation and EBSD mappings are comparable, to elucidate the relative hardness of individual phases. The roles of transformation of phases and hardness per phase on hardening during compression are conveyed in this paper. These comprehensive results are presented as discussed as necessary for the development of crystal plasticity models able to partition strain accommodation by individual phases in complex high entropy alloys. Predicting overall mechanical performance of such alloys requires the guidance and validation in terms of phase specific mechanical properties.

2. Experimental Procedures

2.1 Material processing

The HEA rolled plate's composition studied in the present work was $Fe_{42}Mn_{28}Co_{10}Cr_{15}Si_5$ in atomic percent. The plate was manufactured at Sophisticated Alloys Inc. An ingot of 50.8 mm in thickness was cast and then heat treated at 1100℃ for two hours to achieve homogenization of the structure. After the heat treatment, the material was rolled into a plate 8.9 mm in thickness in multiple passes.

2.2 Mechanical testing

Wire electric discharge machining (EDM) was utilized to make specimens for compression testing, while tensile dog-bone specimens were machined using a lathe. Compression stress-strain data was taken from our earlier work [11]. Two additional cylindrical specimens 3 mm in diameter and 4.8 mm in height were deformed to 0.21 compressive strain and to fracture for microstructural characterization and nanoindentation. Tensile specimens were made with an axis in-plane (IP) aligned with the plate rolling direction (RD). The gauge section of the dog-bone specimens was 28 mm in length and 5 mm in diameter. An MTS biaxial servohydraulic machine of 250 kN capacity was used to perform the tensile tests at room temperature under a constant strain rate of 10^{-3}/s. An MTS 623.12E-24 extensometer was used to measure displacement. Three tensile tests were performed to fracture to ensure reputability of the results. The measured curves were on top of each other.

2.3 Microstructural characterization

Optical microscopy and EBSD using a scanning electron microscope (SEM) were used to determine and characterize the microstructure of the alloy. Optical images were taken using an Olympus OLS5000 microscope. The images were taken using either laser or visible light. EBSD was performed using a Tescan Lyra (Ga) field emission SEM. Scans were taken in field mode with a beam intensity (BI) of 20.05-20.07 at a voltage of 20kV. The working distance was set at 9 mm and the scans were conducted at 615 fps at a 16 x16 bin size. Multiple scans were taken for each strain level to ensure repeatability of the results. All scans contained over 600,000 points with a step size of 0.4 µm. Post processing of the data was performed using OIM analysis software package.

Samples from all strain levels were prepared by grinding with 320, 400, 600, 800, and 1200 grit SiC papers with 6lb force per sample till plane. Post grinding, the samples were polished with a TriDent mat using 3 µm diamond suspension at 150 rpm for 5 minutes, followed by a TriDent mat with 1 µm diamond suspension at 150 rpm for 5 minutes. Lastly, vibratory polishing with a 0.05 µm colloidal silica suspension for 12 hours was conducted to ensure preferable indexing and high confidence index (CI) on the EBSD scans. No etching was necessary after vibratory polishing.

Energy dispersive spectroscopy (EDS) was also completed to observe the elemental composition of phases that were present.

Finally, NeD was completed in Los Alamos Neutron Science Center at Los Alamos National Laboratory for a few specimens, initial and deformed in compression [11, 33-40]. Maud software was used to analyze the experimental data to obtain orientation distributions. Pole figures were plotted in MTEX.

2.4 Nanoindentation

Nanoindentation is a tool for exploring mechanical behavior at small length scales [41]. The technique interrogates materials locally and is only semi-destructive, while allowing extraction of diverse properties including elastic and plastic. Nanoindentation was performed using a KLA Instruments iMicro Nano indenter with a Berkovich tip. Each specimen was initially marked in four corners with a large indentation before EBSD was taken. After EBSD, each specimen was placed into the nano indenter to measure hardness maps in the same area as the EBSD scan took place. The technique results in correlated EBSD and nanoindentation mapping. Areas of 150 µm x 150 µm were always chosen for indenting inside each sample EBSD scan. Using Nanoblitz 3D, a built in KLA indenting function, 22,500 indents were placed in the 150x150 grid with a 1 µm spacing at a force of 750 µN per specimen. Hardness maps, Young's modulus, and correlated phase hardness maps were produced using KLA's post processing software.

The process of NanoBlitz 3D nanoindentation involves forcing the Berkovich tip into the surface of an investigated material. An indentation load (P) is applied as a constant while the resulting indentation depth and contact stiffness are continuously recorded by the instrument. The measured values per indent are then converted into elastic modulus and hardness through the

Oliver-Pharr indentation equations [32]. To this end, the analysis of the load and displacement by the instrument yields a contact penetration depth (h_c) and corresponding contact area ($A_c = \hat{A}_c(h_c)$) per indent to obtain Young's modulus ($E_{IIT} = (1-\upsilon_s^2)\left[\frac{2}{S}\sqrt{\frac{A_c}{\pi}} - \frac{1-\upsilon_i^2}{E_i}\right]$) and hardness ($H_{IIT} = \frac{P_{max}}{A_c}$), where subscripts i and s correspond to indenter and sample. S is beginning of the unloading slope or contact stiffness, $\frac{dP}{dh}|_{h_{max}}$, when the indenter just begins to withdraw from the material. Although the calculation of Young's modulus requires knowledge of the sample's Poisson's ratio, υ_s, the dependence on υ_s is weak. The obtained hardness relating the force on the indenter to the projected contact area per indent is referred to as instrumented indentation testing (IIT) hardness. IIT is sometimes called high speed nanoindentation or high throughput nanoindentation. Evidently, IIT determines material properties without the need to measure the contact area upon where the indenter is withdrawn from the material. Knowing the contact depth over which the probe contacts the material, the contact area, A_c, can be calculated through an area function, $\hat{A}_c(h_c)$. The function is dependent on the geometry of the probe. For the Berkovich tip indenter, which is a three-sided pyramid made of diamond, the function is: $A_c = 24.56h_c^2 + Ch_c$ with C = 150 nm.

Vickers (or Knoop) hardness (HV) can also be obtained by using the mean contact area or Meyer hardness conversion through the KLA iMicro indenter software using: HV $= 94.52 \cdot H_{IIT}$. In contrast to HV governed by ISO 6507 and ASTM E384, IIT governed by ISO 14577 and ASTM E2546 is fast (~1 second per indent). Standard HV relies on a 4-sided Vickers pyramid to obtain one value of hardness at a single force and penetration depth. HV hardness is a ratio of an applied load (kg) to the surface contact area between the indenter and the sample. In contrast, IIT uses a 3-sided Berkovich pyramid probe. Young's modulus and hardness maps are obtained effectively and can be analyzed statistically. IIT is a technique developed for performing large numbers of indentations in short periods of time. Indents are performed over a user defined grid.

To produce high quality property maps over a user defined grid, the considerations of load level and resulting indentation depth, stress fields, and underlying elastic and plastic zones underneath the indenter are important. While the entire elastic zone is sufficient for the modulus measurements, the elastic–plastic deformation zone is required for the hardness measurements. The fields from neighboring indents should not overlap. Therefore, consideration of grid resolution is also important and needs to be carefully defined. We have explored multiple grids while establishing appropriate in-plane indentation spacing between indents to obtain high quality maps presented in the results section of the paper.

3. Results

3.1 Mechanical testing for overall properties

True stress – true strain curves are recorded during compression along the through-thickness (TT)/ND and in-plane (IP)/RD and in tension along RD for the as rolled materials (Fig. 1). As observable, the specimen in IP condition exhibits larger amounts of ductility. The material is approximately isotropic and can accumulate more compressive strain in IP than in TT. The ultimate strength between IP and TT samples are alike, where IP is slightly higher at 1300 MPa while TT has an ultimate strength of 1250 MPa. The material in tension has a yield stress of about 300 MPa and an ultimate tensile strength (UTS) of 520 MPa. The material exhibits poor ductility. To justify the strength and hardening behavior of the material undergoing substantial phase transformation during deformation, microscopy, and nanoindentation characterizations were carried out for establishing phase-hardness correlations, as presented in the following sections.

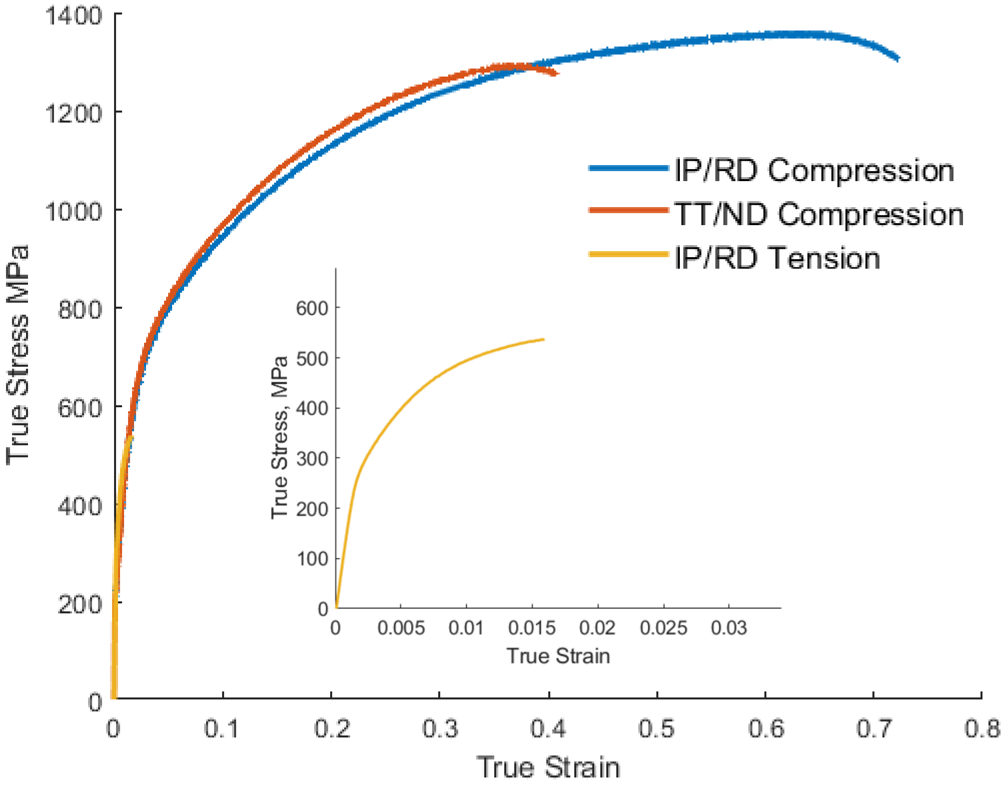

Fig. 1: True stress – true strain curves for the as-rolled specimens of the alloy tested along IP and TT directions in compression and along IP direction in tension to fracture. The plot of the tensile curve is zoomed in for clarity.

3.2 Microstructural characteristics

Inverse pole figure (IPF) maps and corresponding phase maps of the alloy are shown in Fig. 2 for the TT direction. Four phases are identified with green, red, yellow, and blue colors which correspond to γ-austenite, ε-martensite, σ-sigma, and α-ferrite phases, respectively. The lattice parameters are: a_{gamma} = 3.62 Å, a_{sigma} = 8.87 Å and c_{sigma} = 4.64 Å, and $a_{epsilon}$ = 2.60 Å and $c_{epsilon}$ = 4.18 Å [42-44]. We would like to point out that ferrite phase designation is specific to one of the BCC phases in steels. Since our material has quite a complex composition which is not exactly steel, simply calling the ferrite phase as BCC phase may be more appropriate. From the perspective of indexing and determining the type of lattice giving the best fit for a given pattern in EBSD, α-ferrite, δ-ferrite, or α-martensite have no difference because they all have similar lattice constants. As will be shown shortly in an image quality (IQ) map, the BCC phase in the HEA is not the α-martensitic because the intensity is low. Phase fractions based on multiple maps are indicated in the caption. The as-received initial material consists predominantly of γ phase with α being the least prevalent. The average grain size for γ was estimated to be 20 μm for the as rolled samples.

Another IPF map along with its phase map, and an energy dispersive spectroscopy (EDS) elemental map was taken. Luckily the map included more of the BCC phase, and we selected it to perform nanoindentation as indicated in the phase map. γ-austenite and ε-martensite are a solid solution of all 5 elements (Fe, Mn, Co, Cr, Si), and σ-phase is an intermetallic with increased Cr content in a tetragonal structure. Further analyses showed that the σ phase also has a higher Si content. Interestingly, the BCC phase also shows more of Cr. We have added a black overlay highlight for the BCC phase in the Cr composition map. With a higher percentage of Cr in wt%, there is a higher probability of σ-sigma phase forming in stainless steels [45]. In our case, using Si in addition to Cr in higher amounts for Fe-Mn-Co-Cr systems turned out that we got more σ-sigma precipitation [46, 47]. The kernel average misorientation (KAM) map of the initial structure shows a slightly higher presence of geometrically necessary dislocations (GNDs) in the σ-phase relative to the other phases.

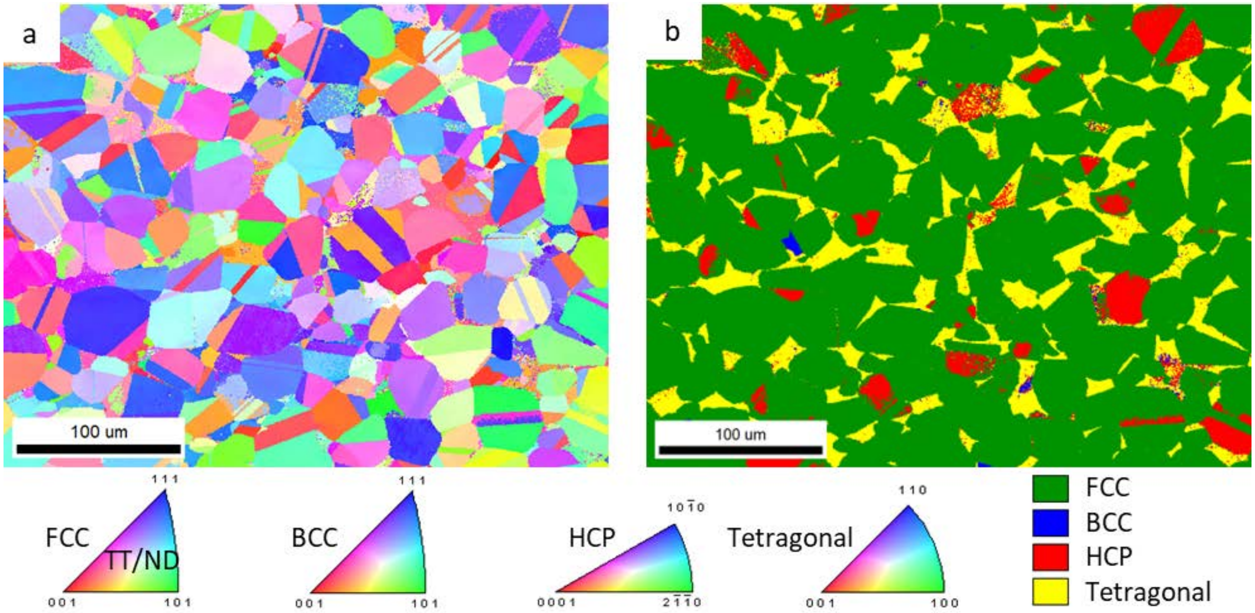

Fig. 2: (a) IPF and (b) phase maps for a specimen of the as-rolled HEA plate. Perpendicular to the maps is the sample TT direction. The colors in the IPF map represent the orientation of the TT/ND plate axis with respect to the crystal lattice frames according to the coloring in the standard IPF triangles per phase. Multiple maps are used to determine the initial average phase fractions: FCC: 78.4%, HCP: 6.2%, BCC: 0.4%, and Tetragonal: 15.0%.

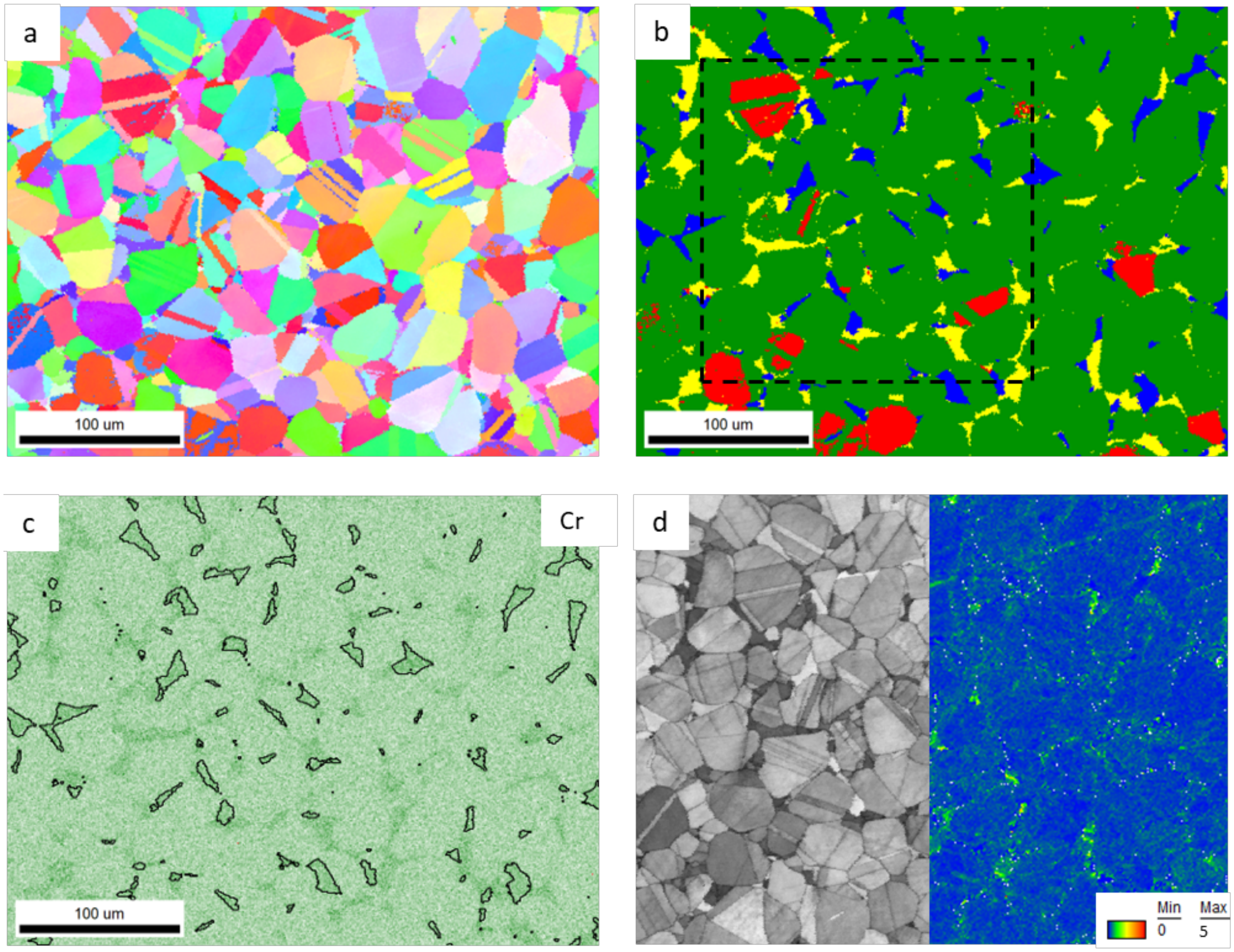

Fig. 3: (a) IPF, (b) phase, (c) EDS Cr composition, (d) half IQ and half KAM maps for a specimen of the as-rolled HEA plate. The frames and colors in the IPF map are the same as those in Fig. 1. The colors in the phase map are the same as those in Fig. 1. The composition map reveals a higher Cr content in the BCC and Tetragonal phases. The IQ and KAM maps show relatively low dislocation density in all phases.

Fig. 4 shows the structure in the alloy at an intermediate strain level and at fracture using IPF and phase maps. Substantial refinement of the structure due to the transformation γ→ε can be observed. The maps show slip bands in γ as sheaves of parallel laths that are strung out on the {111}γ planes carrying out the strain-induced γ→ε martensite transformation. Increasing the content of interfaces in the microstructure with the refinement during deformation increases barriers to mobile dislocations. Such hardening mechanisms are referred to as the dynamic Hall-Petch-type effect. The ability of the alloy to plasticity deform is exhausted with near completion of the transformation. Fig. 5 shows the extent of the transformation with plastic strain under compression measured using EBSD. Crystal orientations with their < 001 > axes parallel to a compression direction easily transform, while crystal orientations compressed around < 011 > and < 111 > cannot transform under compression [48, 49]. The KAM maps of the deformed structures are shown in Fig. 6. Evidently, the presence of GNDs increases in the transforming and deforming phases, ε and γ, while it is smaller in the σ phase. Increased content of dislocations contributes to the local hardness of the phases and also the overall hardening of the alloy.

Fig. 7 shows pole figures of the initial and deformed structures per phase. Texture in the γ phase features the formation of the $\{110\}_\gamma$ fiber as expected for compressive of an FCC material [50-58]. The texture evolution in the ε phase is mainly driven by the TRIP mechanism. The relationship between orientations in the parent γ and child ε phases is $\{111\}_\gamma\{0001\}_\varepsilon$, $\langle 110\rangle_\gamma\langle 2\bar{1}\bar{1}0\rangle_\varepsilon$ [59, 60]. Additionally, these two phases are co-deforming by crystallographic slip [61-64]. Finally, the texture in the σ phase is relatively random and remains such during the compression deformation because the phase does not deform plastically but only floats in the matrix.

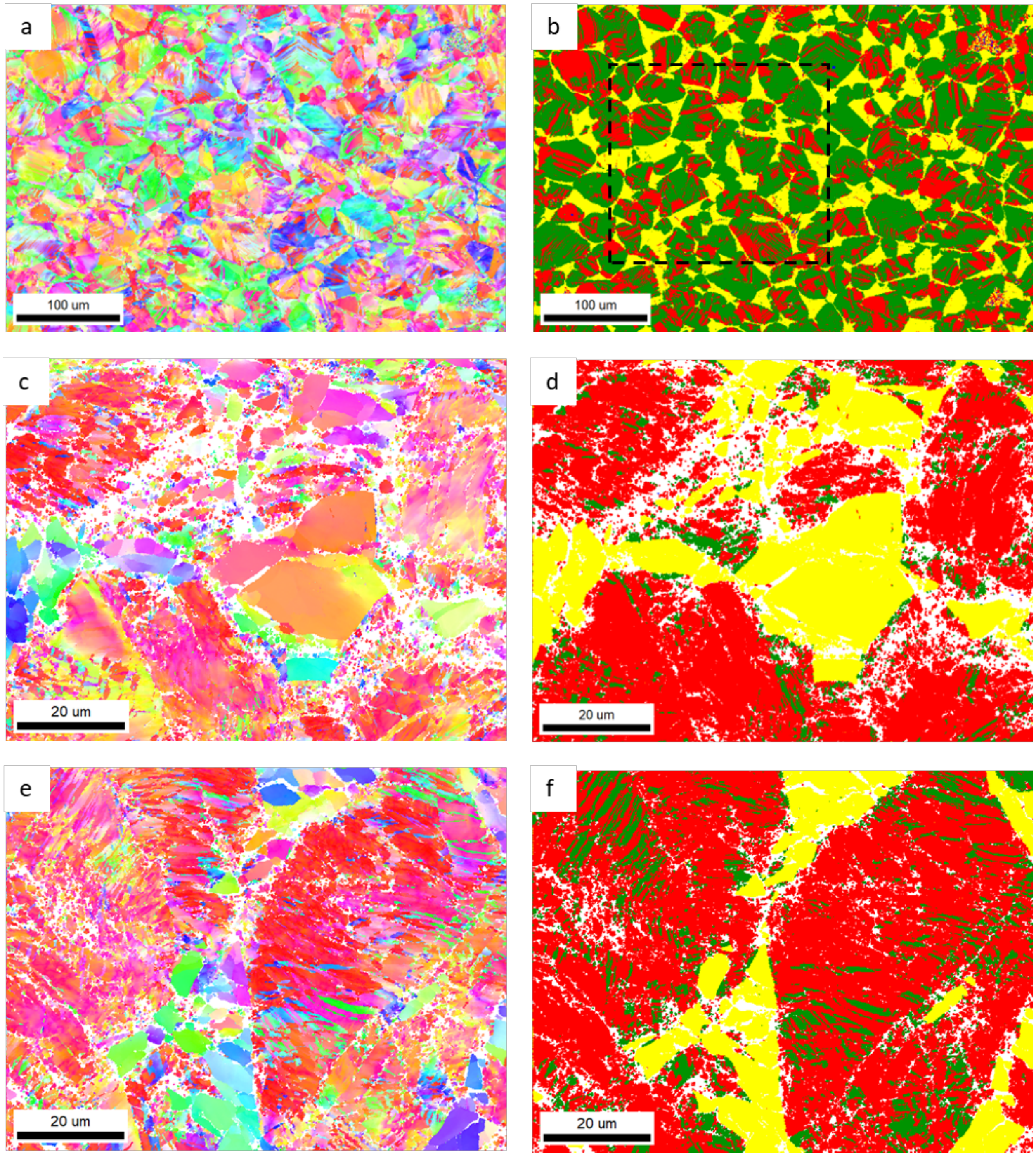

Fig. 4: (a, c, e) IPF and (b, d, f) phase maps for: (a, b) a specimen compressed to 0.21 true strain along TT and (c-f) a specimen compressed to fracture along TT (~0.43 true strain). The frames and colors in the IPF maps are the same as those in Fig. 1. The colors in the phase maps are the same as those in Fig. 1. Multiple maps are used to determine the average phase fractions at 0.21: FCC: 53%, HCP: 32%, BCC: 0%, and Tetragonal: 15.0%, while at 0.43: FCC: 12%, HCP: 73%, BCC: 0%, and Tetragonal: 15.0%.

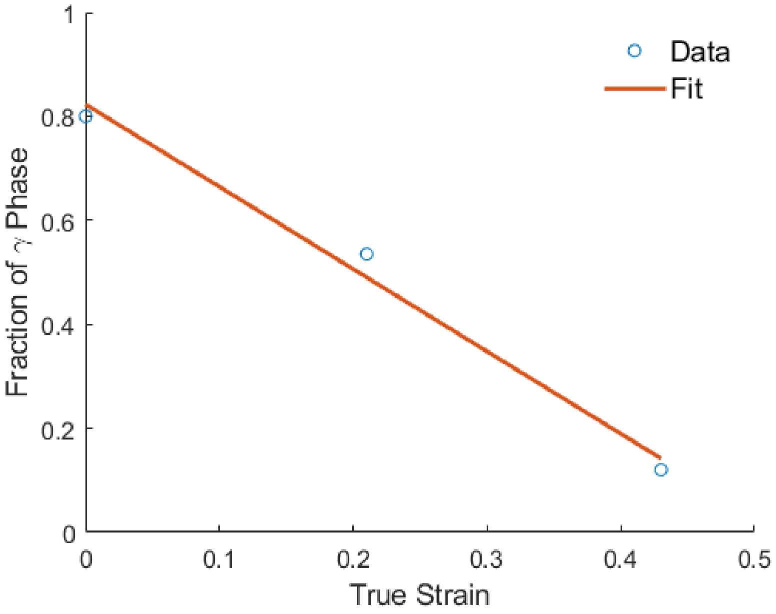

Fig. 5: γ→ε phase fraction transformation from as-rolled material to fracture along TT. The fit is y = -1.48x + 0.82.

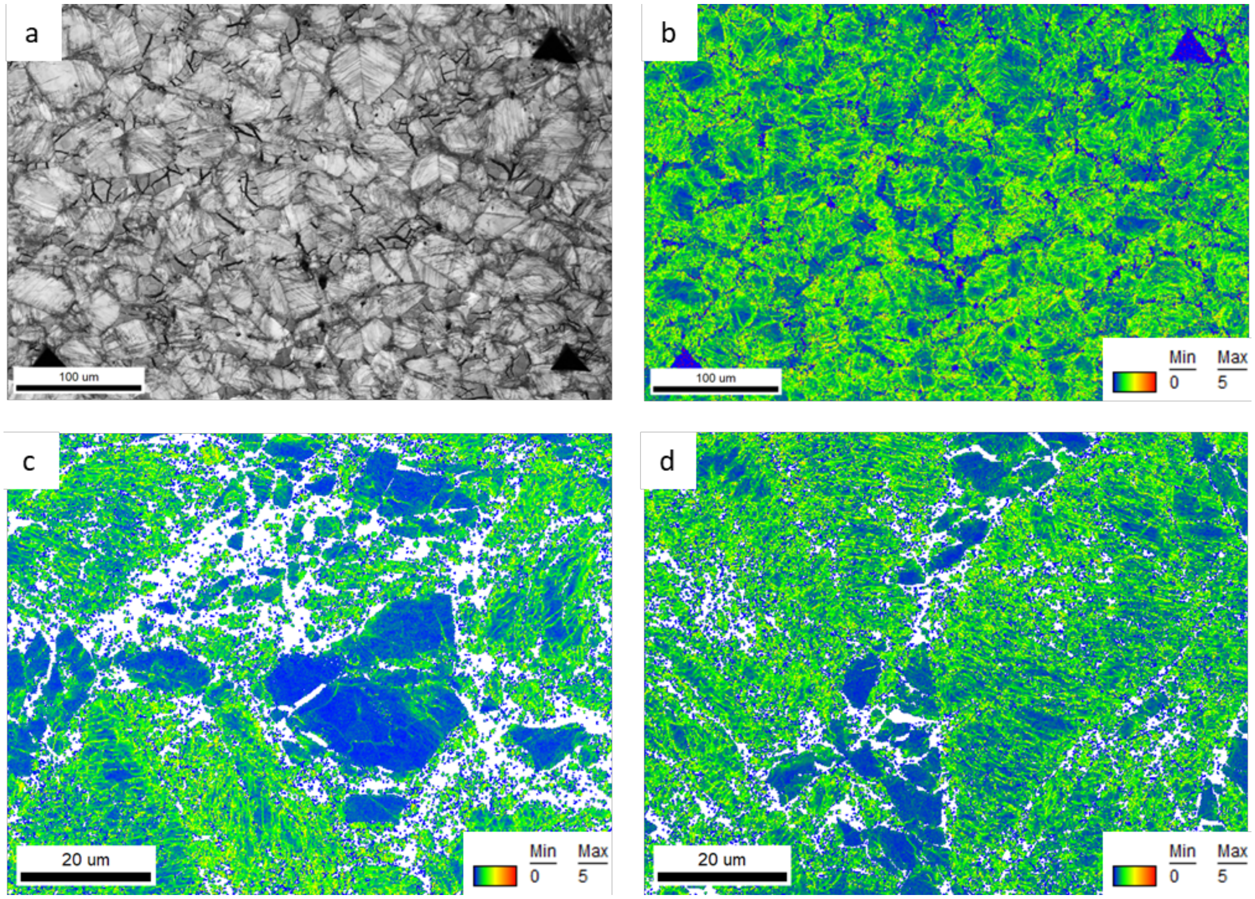

Fig. 6: (a) IQ and (b) KAM maps corresponding to the IPF and phase maps in Fig. 4a and b. (c, d) KAM maps corresponding to the IPF and phase maps in Fig. 4c-f.

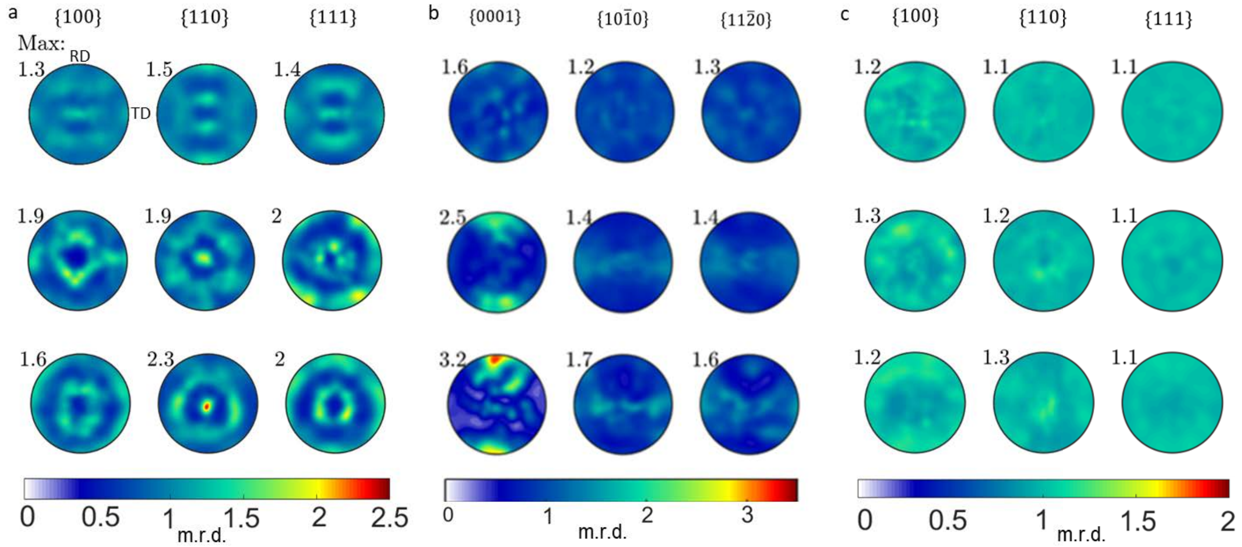

Fig. 7: Stereographic pole figures measured by NeD revealing the evolution of texture per phase in the alloy during compression from initial (top row), to a strain of 0.21 (middle row), and to a strain of 0.43 (bottom row) in (a) austenite, (b) epsilon martensite, and (c) sigma phases.

3.3 Correlated EBSD and nanoindentation mapping for local properties

Initial and strained specimens are subjected to nanoindentation along the TT direction. Two 150x150 μm maps containing 22,500 individual indentations are presented. Appendix A discusses the role of resolution on the results in detail. Fig. 8 displays phase, hardness, correlated phase and hardness, and Young's modulus maps for an initial as-rolled specimen. These maps are the same inner dashed area displayed in Fig. 3b. The KLA software could not distinguish between γ and ε phases based upon hardness alone due to their relative hardness being similar to one another. Integrated software threshold methods to try to separate γ and ε were attempted but were found to be too inaccurate with respect to EBSD phase fraction findings, and therefore their relative hardness were calculated together. Fig. 4c shows this phenomenon where only three colors, blue (γ and ε), pink (BCC), and yellow (σ) are shown. σ has the highest hardness. Table 1 presents the average values. The values were verified by performing individual indents per phase using the instrument in both load and displacement control. For reference, the crystal elastic stiffness constants in GPa for γ-austenite are $C_{11} = 209.0$, $C_{44} = 121.0$, and $C_{12} = 133.0$ [65, 66], for ε-martensite are $C_{11} = 268.7$, $C_{33} = 319.7$, $C_{55} = 49.26$, $C_{12} = 128.6$, and $C_{13} = 77.67$ [67, 68], and for σ are $C_{11} = 452.3$, $C_{33} = 495.6$, $C_{44} = 110.0$, $C_{66} = 111.8$, $C_{12} = 194.2$, and $C_{13} = 157.0$ [69, 70].

Next, measurements of hardness at a higher strain level were conducted. The same procedure as discussed in Fig. 8 was administered for a second specimen pre-compressed to a strain of 0.21. Fig. 9 displays phase, hardness, and correlated phase and hardness maps. These maps are over the same inner dashed area displayed in Fig. 4b. Multiple attempts were made to find and indent the deformed BCC phase, but the phase was never found due to its small volume fraction in the alloy. As for the as-received sample, Fig. 9c correlates phase fractions based upon hardness values. Again, distinguishing between the hardness of γ and ε phases shown in blue was not possible. The relative hardness of γ and ε increased with increasing strain and increased phase fraction of ε. In contrast, the hardness of σ decreased, which is an interesting finding. The finding will be rationalized shortly. Table 2 presents the averaged values. These values were also verified by performing individual indents per phase using the instrument in both load and displacement control.

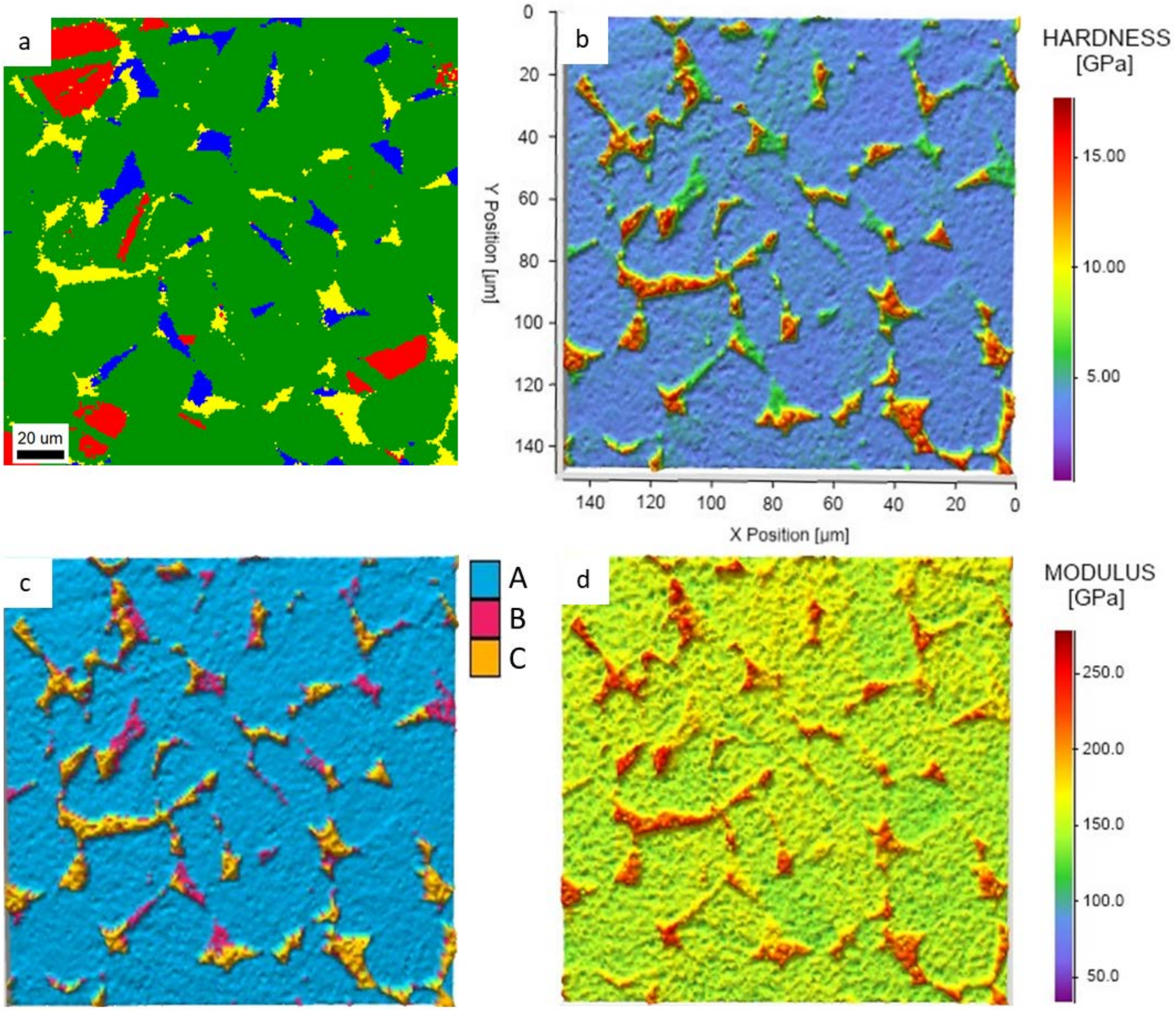

Fig. 8: (a) A sub area of the phase map from Fig. 3b used for nanoindentation to obtain: (b) a hardness map, (c) a correlated phase and hardness map, and (d) a Young's modulus map.

Table 1. H_{IIT} and E_{IIT} along with their standard deviation (STDEV) per phase.

Phase	Hardness Mean [GPa]	Hardness STDEV	Modulus Mean [GPa]	Modulus STDEV
A	3.563	0.479	119.2	8.62

B	7.009	0.348	149.4	6.92
C	13.380	1.056	208.5	12.7

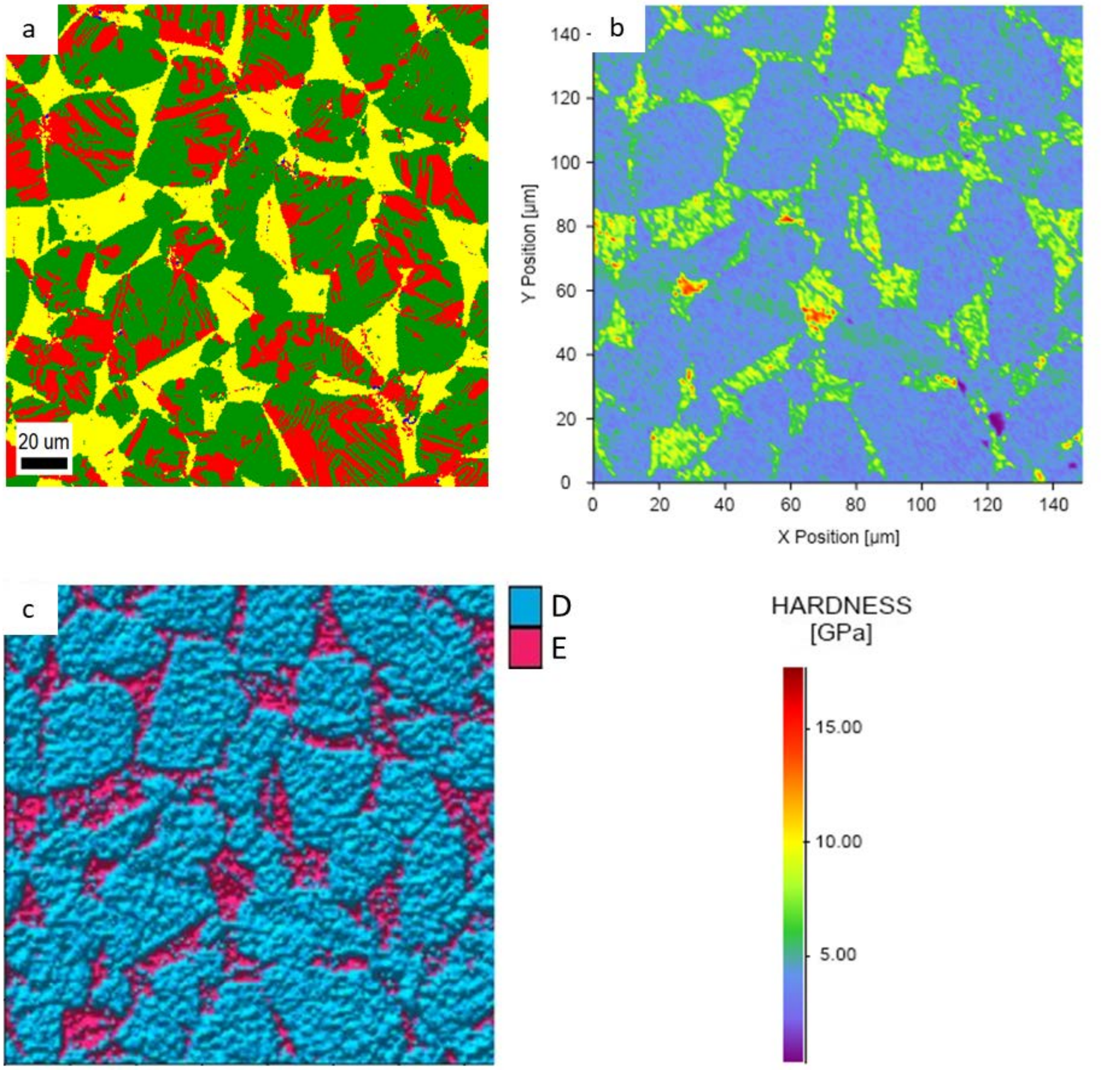

Fig. 9: (a) A sub area of the phase map from Fig. 4b used for nanoindentation to obtain: (b) a hardness map and (c) a correlated phase and hardness map.

.

Table 2. H_{IIT} and E_{IIT} along with their standard deviation per phase.

Phase	Hardness Mean [GPa]	Hardness STDEV
D	4.114	0.589
E	8.145	1.699

4. Discussion

Results presented in the previous section in terms of the evolution of microstructure and local behavior of the alloy are used to rationalize and interpret the overall hardening behavior of the alloy. Since nano-hardness response at every individual indent steams from localized microstructural heterogeneities, contributions from strengthening mechanisms such as dislocations and solid solutions to the overall strength can be inferred [71, 72]. In the present study, nano indentation is used to rule out the contribution of dislocation buildups to the strength of the alloy. Phases γ and ε are found to exhibit similar hardness with plastic straining revealing that increasing the fraction of the dislocated ε phase during deformation due to the transformation is not a primary source of strain hardening. Nevertheless, both γ and ε phases exhibit moderate hardening owing to the increase in dislocation density. Measurements suggest an increase in strength due to dislocations of about 15%. Table 3 presents estimated HV based on the H_{IIT} measurements. The relationship between HV and flow stress can be approximated using Tabors equation where HV is first converted from kg_f/mm^2 to MPa by multiplying the HV values by 9.80665 and then dividing by a factor of ~4 or so. In doing so, the initial yield stress of the alloy would be 820 MPa, while that at 0.21 true strain would be 950 MPa based on the HV values for the FCC/HCP phases. The actual yielding of the alloy under compression is at about 600 MPa, while flow strength at 0.21 true strain is 1180 MPa. Evidently, estimates based on HV are inaccurate as is often the case for multi-phase materials. Therefore, the origin of the strength differential from yielding to that at 0.21 true strain can not be owing to solely dislocation driven hardening of individual phase.

The refinement of the structure during the transformation inducing a dynamic Hall-Petch-type barrier effect is a primary source of hardening in the alloy. Restricting the slip length associated with dislocations in γ and ε is found very effective in strain hardening of the alloy. Effective strengthening by structural refinement has been achieved in many HEAs [73, 74].

Moreover, some load transfer between phases contribution to strengthening likely operates under deformation, given the composite structure of the alloy. Such contribution is driven by the volume fraction, morphology, and strength/stiffness of the reinforcement σ phase [75-80]. Fig. 10 shows images of the structure revealing networks of cracks developing in the σ phase during compression. The σ phase does not deform/reorientate/float but interestingly begins to crack and fragment with plastic strain. The fragments float around in the surrounding γ and ε matrix. It is found that the hardness of the σ phase decreased with the plastic strain in compression. The decrease in the relative hardness of σ is because the nano indenter tip deflects from the cracked floating phase in the surrounding matrix instead of loading uniaxially. As a result of such softening, any load transfer hardening would decrease.

The present study confirmed that the high throughput nanoindentation mapping is an effective way to characterize the relative strength of phases in multi-phase materials. Large quantities of identical tests were performed within relatively short timescales as compared to more traditional methods [81, 82]. While the technique can probe even more complex microstructures consisting of dislocation structures or nanotwins at nano and micro scales, results attained in the present study show nano-hardness per phase and the evolution of hardness per phase during deformation. The increase/decrease in the relative strength per phases was determined for the $Fe_{42}Mn_{28}Co_{10}Cr_{15}Si_5$ (in at%) HEA. However, there are some limitations of the nanoindentation mapping approach. For example, distinguishing separate phases based upon hardness is not possible for phases with similar hardness values, like γ and ε in the present work. Measured values are useful to compare the relative strength of phases while the actual strength cannot be measured. Nevertheless, assessing relative strength between phases is very useful for the development of crystal plasticity models for multi-phase materials [83-89]. Given the relative strength per phase, the models would be enabled to partition plastic strain accommodation by individual phases in complex high entropy alloys. The combination of nanoindentation experimental approach and advanced crystal plasticity modeling handling phase transformations approach [90-95] can determine strength per phase along with the evolution of strength and microstructure. The approach will be pursued in future works.

In closing, we show fractography of the specimen pulled to fracture in tension. Brittle micromechanisms of fracture can be observed owing to the brittle σ phase. The fracture surface consists of a rough intergranular fracture with some transgranular facets from grain to grain.

Table 3. Estimated HV in kg_f/mm^2 from H_{IIT} in GPa.

Phase	Initial	$\varepsilon = 0.21$
FCC	336	389
HCP	336	389
Tetragonal	1264	769
BCC	662	N/A

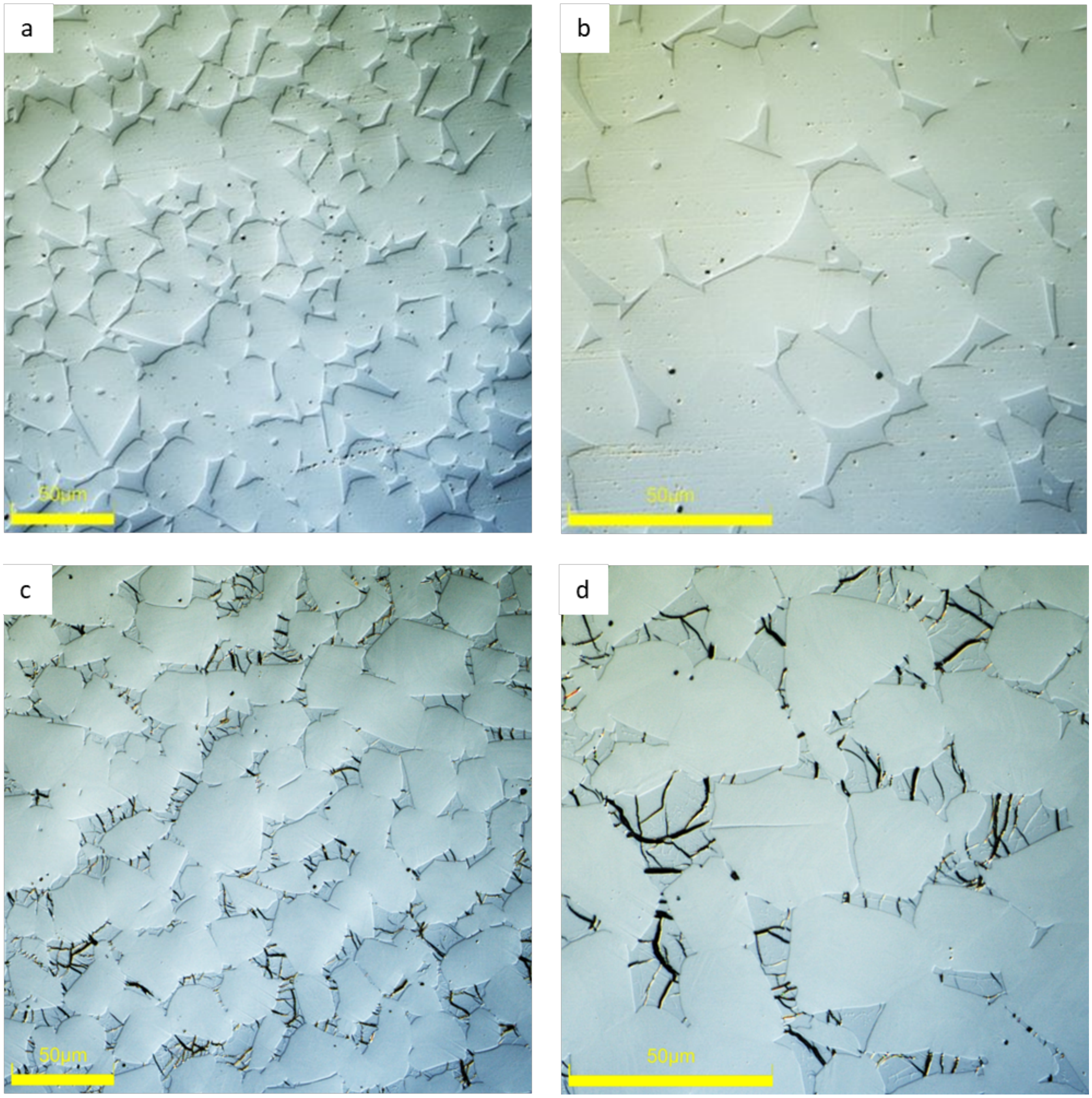

Fig. 10: Optical microscopy images of (a, b) an undeformed initial specimen and (c, d) a compressed specimen along TT to a strain of 0.21. Note networks of cracks developed in sigma phase after the compression. Perpendicular to the images is the sample TT direction. The scale bars are 50 µm.

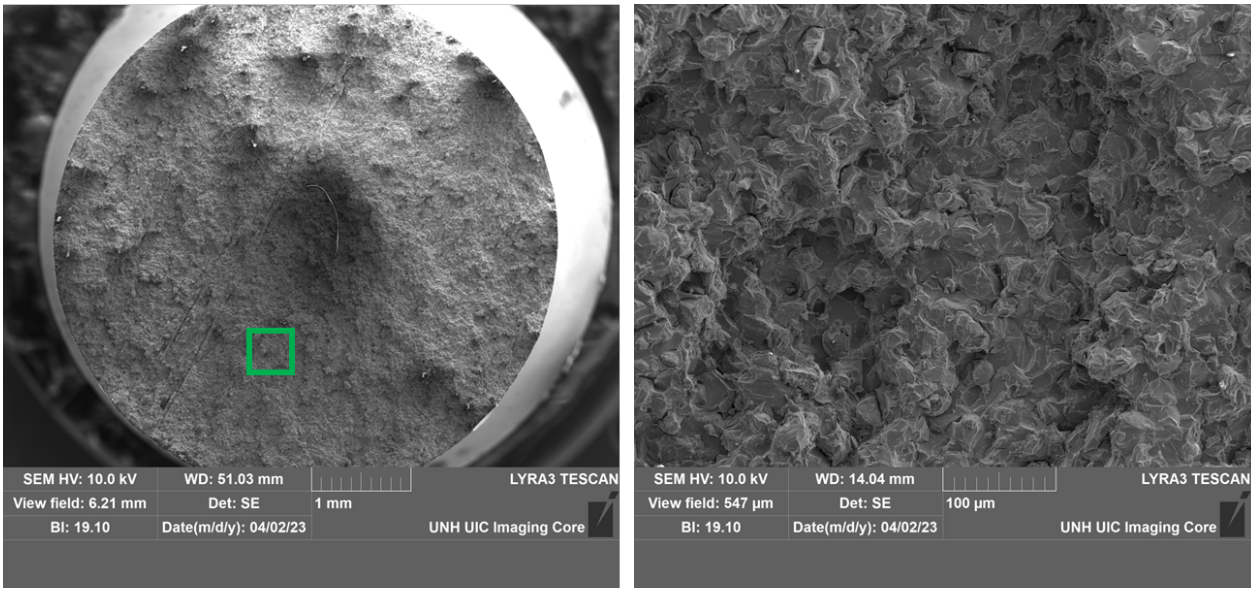

Fig. 11: Secondary electron images showing the fracture surface for a specimen pulled in tension to fracture along RD.

5. Conclusions

In this work, we have characterized the evolution microstructure undergoing strain induced $\gamma \rightarrow \varepsilon$ phase transformation and measured overall strength/ductility in tension and compression along with localized hardness/strength per phase in a quadruplex HEA, $Fe_{42}Mn_{28}Co_{10}Cr_{15}Si_5$ (in at%). The material was investigated in its as-received state and after plastic straining under compression. The emphasis was on assessing the evolution of relative hardness/strength between individual phases via high-throughput nanoindentation to clarify the origins of strain hardening of the alloy. The main conclusions of the study are:

- The overall behavior of the alloy in compression features a great deal of plasticity and strain hardening before fracture. The plasticity is accommodated through the strain induced $\gamma \rightarrow \varepsilon$ phase transformation to near completion along with dislocation slip in metastable γ and stable ε phases.
- Phases γ and ε are found to exhibit similar hardness with plastic straining revealing that increasing the fraction of the dislocated ε phase during deformation due to transformation is not a primary source of strain hardening. Nevertheless, both γ and ε phases exhibit moderate hardening owing to the increase in dislocation density.
- The contents of diffusion created σ phase remains constant during deformation. The phase floats in the surrounding matrix before beginning to crack at higher strain levels. Cracking and fragmentation of the phase during deformation causes localized softening but not early fracture under compression.
- The primary source of strain hardening in the alloy is the refinement of the structure during the transformation inducing a dynamic Hall-Petch-type barrier effect. The secondary sources are owing to the build up of dislocations in the γ and ε phases with plastic strain and to some load transfer because of the strength/stiffness differential between constituent phases.

- The alloy is found to behave poorly under tension. Fracture surfaces after tension feature brittle micromechanisms of fracture. Such behavior is attributed to the presence of the brittle σ phase. Future work will focus on designing new compositions to suppress the occurrence of the σ phase.

Acknowledgements

This research was supported by the DEVCOM Army Research Laboratory under cooperative agreement no. W911NF-21-2-0149 and the U.S. National Science Foundation under grant no. OIA-1757371.

Data availability

The raw/processed data required to reproduce these findings cannot be shared at this time due to technical or time limitations.

Appendix

Because conducting high-speed nanoindentation mapping and interpreting its results requires appropriate indentation spacing and indentation depth, this appendix presents indents/imprints in specimens after nanoindentation. The results are shown at two applied force levels, 750 μN and 1750 μN. Spacing between indents was 1 μm for both loads, as recommended for sufficient resolution contour plots. The spacing is defined as the distance between the center of one indent to the center of the next. The spacing must also be optimized to prohibit interference between adjacent indents while maximizing indentation coverage for contours of properties over the given grain structures. 0.5 μm between the most right corner of one indent to the most left corner of another is recommended as optimal to allow for the indents to be as close to one another as possible without interfering. While we have explored broad ranges of spacings and forces for achieving good looking and accurate maps, we chose to show indents under two forces in Fig. A1. Results based on the two loads were very similar and within the standard deviation. However, we regard the second force as an upper bound for achieving accurate results in both phases simultaneously for 1 μm spacing because the indents begin to interact in the FCC/HCP phases. Further increase in the load would still provide accurate measurements in the Tetragonal phase but not in the FCC/HCP phases. Average depth, h_c, over indents was 105 nm in FCC/HCP, 75 nm in BCC, and 55 nm in Tetragonal under 750 μN, while 135 nm in FCC/HCP and 70 nm in Tetragonal under 1750 μN force. The 22,500 indent maps took 6.15 hours to complete, which is approximately 1 second per indent.

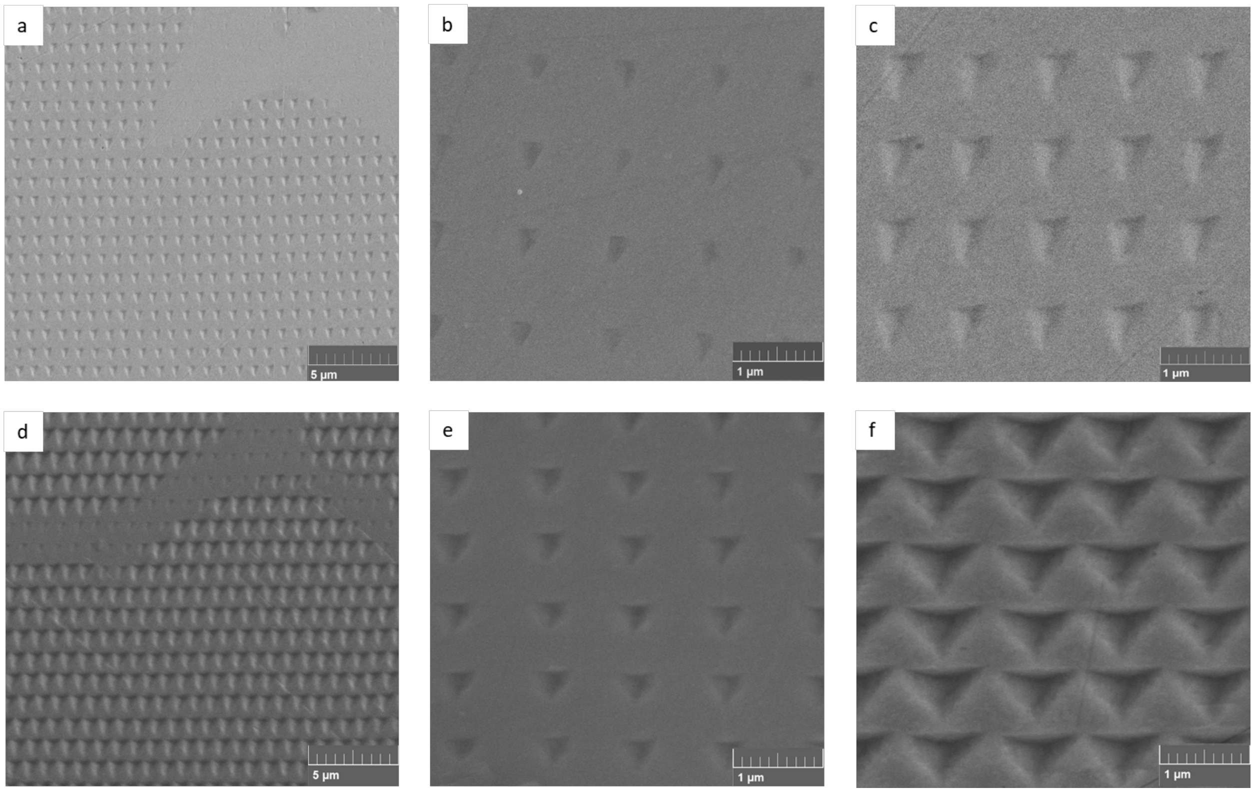

Fig. A1: Secondary electrons images showing indents under (a, b, c) 750 µN force and (d, e, f) 1750 µN force. (b) is a magnified region from (a) in σ phase. (c) is a magnified region from (a) in γ and ε phases. (e) is a magnified region from (d) in σ phase. (f) is a magnified region from (d) in γ and ε phases.

References

[1] B. Cantor, Multicomponent and high entropy alloys, Entropy, 16 (2014) 4749-4768.
[2] J.W. Yeh, S.K. Chen, S.J. Lin, J.Y. Gan, T.S. Chin, T.T. Shun, C.H. Tsau, S.Y. Chang, Nanostructured high-entropy alloys with multiple principal elements: novel alloy design concepts and outcomes, Advanced Engineering Materials, 6 (2004) 299-303.
[3] B. Cantor, Multicomponent and High Entropy Alloys, Entropy, 2014, pp. 4749-4768.
[4] J. Weiss, D.J. Savage, S.C. Vogel, B.A. McWilliams, R.S. Mishra, M. Knezevic, Evolution of microstructure and strength of a high entropy alloy undergoing the strain-induced martensitic transformation, Mater. Sci. Eng. A, 887 (2023) 145754.
[5] Z. Li, K.G. Pradeep, Y. Deng, D. Raabe, C.C. Tasan, Metastable high-entropy dual-phase alloys overcome the strength–ductility trade-off, Nature, 534 (2016) 227-230.
[6] Z. Li, C.C. Tasan, K.G. Pradeep, D. Raabe, A TRIP-assisted dual-phase high-entropy alloy: Grain size and phase fraction effects on deformation behavior, Acta. Mater., 131 (2017) 323-335.
[7] Y. Deng, C.C. Tasan, K.G. Pradeep, H. Springer, A. Kostka, D. Raabe, Design of a twinning-induced plasticity high entropy alloy, Acta Materialia, 94 (2015) 124-133.
[8] Z. Li, D. Raabe, Strong and ductile non-equiatomic high-entropy alloys: design, processing, microstructure, and mechanical properties, Jom, 69 (2017) 2099-2106.

[9] M.J. Yao, K.G. Pradeep, C.C. Tasan, D. Raabe, A novel, single phase, non-equiatomic FeMnNiCoCr high-entropy alloy with exceptional phase stability and tensile ductility, Scripta Materialia, 72-73 (2014) 5-8.
[10] B. He, B. Hu, H. Yen, G. Cheng, Z. Wang, H. Luo, M. Huang, High dislocation density–induced large ductility in deformed and partitioned steels, Science, 357 (2017) 1029-1032.
[11] S. Bhowmik, J. Zhang, S.C. Vogel, S.S. Nene, R.S. Mishra, B.A. McWilliams, M. Knezevic, Effects of plasticity-induced martensitic transformation and grain refinement on the evolution of microstructure and mechanical properties of a metastable high entropy alloy, J. Alloys Compd., 891 (2022) 161871.
[12] Y. Zhang, T.T. Zuo, Z. Tang, M.C. Gao, K.A. Dahmen, P.K. Liaw, Z.P. Lu, Microstructures and properties of high-entropy alloys, Progress in Materials Science, 61 (2014) 1-93.
[13] N. Kumar, M. Komarasamy, P. Nelaturu, Z. Tang, P.K. Liaw, R.S. Mishra, Friction Stir Processing of a High Entropy Alloy Al0.1CoCrFeNi, JOM, 67 (2015) 1007-1013.
[14] E. Galindo-Nava, P. Rivera-Díaz-del-Castillo, Understanding martensite and twin formation in austenitic steels: A model describing TRIP and TWIP effects, Acta Materialia, 128 (2017) 120-134.
[15] R. Xiong, H. Peng, H. Si, W. Zhang, Y. Wen, Thermodynamic calculation of stacking fault energy of the Fe–Mn–Si–C high manganese steels, Materials Science and Engineering: A, 598 (2014) 376-386.
[16] A.K. Nair, E. Parker, P. Gaudreau, D. Farkas, R.D. Kriz, Size effects in indentation response of thin films at the nanoscale: A molecular dynamics study, International Journal of Plasticity, 24 (2008) 2016-2031.
[17] C.J. Ruestes, E.M. Bringa, Y. Gao, H.M. Urbassek, Molecular dynamics modeling of nanoindentation, Applied nanoindentation in advanced materials, (2017) 313-345.
[18] C.J. Ruestes, I.A. Alhafez, H.M. Urbassek, Atomistic studies of nanoindentation—A review of recent advances, Crystals, 7 (2017) 293.
[19] N.X. Randall, M. Vandamme, F.-J. Ulm, Nanoindentation analysis as a two-dimensional tool for mapping the mechanical properties of complex surfaces, Journal of Materials Research, 24 (2009) 679-690.
[20] C. Tromas, M. Arnoux, X. Milhet, Hardness cartography to increase the nanoindentation resolution in heterogeneous materials: Application to a Ni-based single-crystal superalloy, Scr. Mater., 66 (2012) 77-80.
[21] I.A. Alhafez, C.J. Ruestes, E.M. Bringa, H.M. Urbassek, Nanoindentation into a high-entropy alloy–An atomistic study, Journal of Alloys and Compounds, 803 (2019) 618-624.
[22] C.J. Ruestes, D. Farkas, Dislocation emission and propagation under a nano-indenter in a model high entropy alloy, Computational Materials Science, 205 (2022) 111218.
[23] C. Varvenne, A. Luque, W.G. Nöhring, W.A. Curtin, Average-atom interatomic potential for random alloys, Physical Review B, 93 (2016) 104201.
[24] R. Pasianot, D. Farkas, Atomistic modeling of dislocations in a random quinary high-entropy alloy, Computational Materials Science, 173 (2020) 109366.
[25] I. Basu, J.T.M. De Hosson, Strengthening mechanisms in high entropy alloys: fundamental issues, Scripta Materialia, 187 (2020) 148-156.
[26] Y. Qi, H. Xu, T. He, M. Feng, Effect of crystallographic orientation on mechanical properties of single-crystal CoCrFeMnNi high-entropy alloy, Materials Science and Engineering: A, 814 (2021) 141196.

[27] S. Shuang, S. Lu, B. Zhang, C. Bao, Q. Kan, G. Kang, X. Zhang, Effects of high entropy and twin boundary on the nanoindentation of CoCrNiFeMn high-entropy alloy: A molecular dynamics study, Computational Materials Science, 195 (2021) 110495.
[28] D.-Q. Doan, T.-H. Fang, T.-H. Chen, Microstructure and composition dependence of mechanical characteristics of nanoimprinted AlCoCrFeNi high-entropy alloys, Scientific reports, 11 (2021) 1-19.
[29] E.D. Hintsala, U. Hangen, D.D. Stauffer, High-throughput nanoindentation for statistical and spatial property determination, Jom, 70 (2018) 494-503.
[30] Y. Chen, E. Hintsala, N. Li, B.R. Becker, J.Y. Cheng, B. Nowakowski, J. Weaver, D. Stauffer, N.A. Mara, High-throughput nanomechanical screening of phase-specific and temperature-dependent hardness in Al x FeCrNiMn high-entropy alloys, Jom, 71 (2019) 3368-3377.
[31] Q. Fan, K. Gan, D. Yan, Z. Li, Nanoindentation creep behavior of diverse microstructures in a pre-strained interstitial high-entropy alloy by high-throughput mapping, Materials Science and Engineering: A, 856 (2022) 143988.
[32] W.C. Oliver, G.M. Pharr, Improved technique for determining hardness and elastic modulus using load and displacement sensing indentation experiments, Journal of Materials Research, 7 (1992) 1564-1580.
[33] H.-R. Wenk, L. Lutterotti, S. Vogel, Texture analysis with the new HIPPO TOF diffractometer, Nuclear Instruments and Methods in Physics Research Section A: Accelerators, Spectrometers, Detectors and Associated Equipment, 515 (2003) 575-588.
[34] N.C. Ferreri, Z. Feng, D.J. Savage, D.W. Brown, B. Clausen, T.A. Sisneros, M. Knezevic, In-situ high-energy X-ray diffraction and crystal plasticity modeling to predict the evolution of texture, twinning, lattice strains and strength during loading and reloading of beryllium, Int. J. Plast., 150 (2022) 103217.
[35] N.C. Ferreri, S. Ghorbanpour, S. Bhowmik, R. Lussier, J. Bicknell, B.M. Patterson, M. Knezevic, Effects of build orientation and heat treatment on the evolution of microstructure and mechanical properties of alloy Mar-M-509 fabricated via laser powder bed fusion, Int. J. Plast., 121 (2019) 116-133.
[36] N.C. Ferreri, R. Pokharel, V. Livescu, D.W. Brown, M. Knezevic, J.-S. Park, M.A. Torrez, G.T. Gray, Effects of heat treatment and build orientation on the evolution of ϵ and α' martensite and strength during compressive loading of additively manufactured 304L stainless steel, Acta. Mater., 195 (2020) 59-70.
[37] N.C. Ferreri, S.C. Vogel, M. Knezevic, Determining volume fractions of γ, γ', γ'', δ, and MC-carbide phases in Inconel 718 as a function of its processing history using an advanced neutron diffraction procedure, Mater. Sci. Eng. A, 781 (2020) 139228.
[38] N. Matukhno, N. Kljestan, M. Knezevic, Enhancing elongation and trading off strength versus ductility of commercially pure titanium sheets using cyclic bending under tension and annealing, International Journal of Solids and Structures, 276 (2023) 112324.
[39] N. Matukhno, N. Kljestan, S.C. Vogel, M. Knezevic, Cyclic bending under tension of alloy AZ31 sheets: Influence on elongation-to-fracture and strength, Mater. Sci. Eng. A, 857 (2022) 144127.
[40] T.J. Barrett, R.J. McCabe, D.W. Brown, B. Clausen, S.C. Vogel, M. Knezevic, Predicting deformation behavior of α-uranium during tension, compression, load reversal, rolling, and sheet forming using elasto-plastic, multi-level crystal plasticity coupled with finite elements, J. Mech. Phys. Solids, 138 (2020) 103924.

[41] S. Pathak, S.R. Kalidindi, Spherical nanoindentation stress–strain curves, Materials Science and Engineering: R: Reports, 91 (2015) 1-36.
[42] J. Häglund, A. Fernández Guillermet, G. Grimvall, M. Körling, Theory of bonding in transition-metal carbides and nitrides, Physical Review B, 48 (1993) 11685-11691.
[43] G. Bergman, D.P. Shoemaker, The determination of the crystal structure of the [sigma] phase in the iron-chromium and iron-molybdenum systems, Acta Crystallographica, 7 (1954) 857-865.
[44] T.J. Barrett, M. Knezevic, Deep drawing simulations using the finite element method embedding a multi-level crystal plasticity constitutive law: Experimental verification and sensitivity analysis, Computer Methods in Applied Mechanics and Engineering, 354 (2019) 245-270.
[45] T. Liang, X.Q. Hu, X.H. Kang, D.Z. Li, Effect of The Sigma Phase on the Mechanical Properties of a Cast Duplex Stainless Steel during the Ageing Treatment at 850°C, Advanced Materials Research, 684 (2013) 325-329.
[46] S.S. Nene, M. Frank, P. Agrawal, S. Sinha, K. Liu, S. Shukla, R.S. Mishra, B.A. McWilliams, K.C. Cho, Microstructurally flexible high entropy alloys: Linkages between alloy design and deformation behavior, Materials & Design, 194 (2020) 108968.
[47] C.-C. Hsieh, W. Wu, Overview of intermetallic sigma (σ) phase precipitation in stainless steels, International Scholarly Research Notices, 2012 (2012) 732471.
[48] E. Polatidis, W.N. Hsu, M. Šmíd, T. Panzner, S. Chakrabarty, P. Pant, H. Van Swygenhoven, Suppressed martensitic transformation under biaxial loading in low stacking fault energy metastable austenitic steels, Scr. Mater., 147 (2018) 27-32.
[49] D. Goodchild, W.T. Roberts, D.V. Wilson, Plastic deformation and phase transformation in textured austenitic stainless steel, Acta Metall., 18 (1970) 1137-1145.
[50] Z. Feng, R. Pokharel, S.C. Vogel, R.A. Lebensohn, D. Pagan, E. Zepeda-Alarcon, B. Clausen, R. Martinez, G.T. Gray, M. Knezevic, Crystal plasticity modeling of strain-induced martensitic transformations to predict strain rate and temperature sensitive behavior of 304 L steels: Applications to tension, compression, torsion, and impact, Int. J. Plast., 156 (2022) 103367.
[51] M. Knezevic, S.R. Kalidindi, R.K. Mishra, Delineation of first-order closures for plastic properties requiring explicit consideration of strain hardening and crystallographic texture evolution, Int. J. Plast., 24 (2008) 327-342.
[52] M. Knezevic, S.R. Kalidindi, D. Fullwood, Computationally efficient database and spectral interpolation for fully plastic Taylor-type crystal plasticity calculations of face-centered cubic polycrystals, Int. J. Plast., 24 (2008) 1264-1276.
[53] M. Knezevic, H.F. Al-Harbi, S.R. Kalidindi, Crystal plasticity simulations using discrete Fourier transforms, Acta. Mater., 57 (2009) 1777-1784.
[54] M. Knezevic, I.J. Beyerlein, Multiscale Modeling of Microstructure-Property Relationships of Polycrystalline Metals during Thermo-Mechanical Deformation, Advanced Engineering Materials, 20 (2018) 1700956.
[55] M. Zecevic, M. Knezevic, An implicit formulation of the elasto-plastic self-consistent polycrystal plasticity model and its implementation in implicit finite elements, Mechanics of Materials, 136 (2019) 103065.
[56] I.A. Riyad, M. Knezevic, Field fluctuations viscoplastic self-consistent crystal plasticity: Applications to predicting texture evolution during deformation and recrystallization of cubic polycrystalline metals, Acta. Mater., 261 (2023) 119395.

[57] S. Daroju, T. Kuwabara, R. Sharma, D.T. Fullwood, M.P. Miles, M. Knezevic, Experimental characterization and crystal plasticity modeling for predicting load reversals in AA6016-T4 and AA7021-T79, Int. J. Plast., 153 (2022) 103292.
[58] M. Zecevic, T. Roemer, M. Knezevic, Y. Korkolis, B. Kinsey, Residual Ductility and Microstructural Evolution in Continuous-Bending-under-Tension of AA-6022-T4, Materials, 9 (2016) 130.
[59] L. Bracke, L. Kestens, J. Penning, Transformation mechanism of α′-martensite in an austenitic Fe–Mn–C–N alloy, Scr. Mater., 57 (2007) 385-388.
[60] Z. Feng, M. Zecevic, M. Knezevic, Stress-assisted (γ→α′) and strain-induced (γ→ε→α′) phase transformation kinetics laws implemented in a crystal plasticity model for predicting strain path sensitive deformation of austenitic steels, Int. J. Plast., 136 (2021) 102807.
[61] T.J. Barrett, A. Eghtesad, R.J. McCabe, B. Clausen, D.W. Brown, S.C. Vogel, M. Knezevic, A generalized spherical harmonics-based procedure for the interpolation of partial datasets of orientation distributions to enable crystal mechanics-based simulations, Materialia, 6 (2019) 100328.
[62] A. Eghtesad, T.J. Barrett, M. Knezevic, Compact reconstruction of orientation distributions using generalized spherical harmonics to advance large-scale crystal plasticity modeling: Verification using cubic, hexagonal, and orthorhombic polycrystals, Acta. Mater., 155 (2018) 418-432.
[63] R.E. Marki, K.A. Brindley, R.J. McCabe, M. Knezevic, Crystal mechanics-based thermo-elastic constitutive modeling of orthorhombic uranium using generalized spherical harmonics and first-order bounding theories, Journal of Nuclear Materials, 560 (2022) 153472.
[64] M. Knezevic, N.W. Landry, Procedures for reducing large datasets of crystal orientations using generalized spherical harmonics, Mechanics of Materials, 88 (2015) 73-86.
[65] H.M. Ledbetter, Predicted monocrystal elastic constants of 304-type stainless steel, Physica B+C, 128 (1985) 1-4.
[66] M. Knezevic, S.R. Kalidindi, Fast computation of first-order elastic-plastic closures for polycrystalline cubic-orthorhombic microstructures, Comput. Mater. Sci., 39 (2007) 643-648.
[67] S. Pronk, D. Frenkel, Large difference in the elastic properties of fcc and hcp hard-sphere crystals, Physical review letters, 90 (2003) 255501.
[68] N. Landry, M. Knezevic, Delineation of First-Order Elastic Property Closures for Hexagonal Metals Using Fast Fourier Transforms, Materials, 8 (2015) 6326-6345.
[69] K. Kishida, M. Okutani, H. Suzuki, H. Inui, M. Heilmaier, D. Raabe, Room-temperature deformation of single crystals of the sigma-phase compound FeCr with the tetragonal D8b structure investigated by micropillar compression, Acta. Mater., 249 (2023) 118829.
[70] M. Knezevic, L. Capolungo, C.N. Tomé, R.A. Lebensohn, D.J. Alexander, B. Mihaila, R.J. McCabe, Anisotropic stress-strain response and microstructure evolution of textured α-uranium, Acta. Mater., 60 (2012) 702-715.
[71] T. Maity, K.G. Prashanth, Ö. Balcı, J.T. Kim, T. Schöberl, Z. Wang, J. Eckert, Influence of severe straining and strain rate on the evolution of dislocation structures during micro-/nanoindentation in high entropy lamellar eutectics, International Journal of Plasticity, 109 (2018) 121-136.
[72] R.S. Ganji, P.S. Karthik, K.B.S. Rao, K.V. Rajulapati, Strengthening mechanisms in equiatomic ultrafine grained AlCoCrCuFeNi high-entropy alloy studied by micro-and nanoindentation methods, Acta Materialia, 125 (2017) 58-68.

[73] W. Fu, Y. Huang, J. Sun, A.H. Ngan, Strengthening CrFeCoNiMn0. 75Cu0. 25 high entropy alloy via laser shock peening, International Journal of Plasticity, 154 (2022) 103296.
[74] Y. Liu, Y. He, S. Cai, Effect of gradient microstructure on the strength and ductility of medium-entropy alloy processed by severe torsion deformation, Materials Science and Engineering: A, 801 (2021) 140429.
[75] M. Wang, M. Knezevic, M. Chen, Effects of Fe content on microstructure and mechanical properties of Al-Y eutectic alloys, Mater. Sci. Eng. A, 863 (2023) 144558.
[76] R. Casati, Aluminum matrix composites reinforced with alumina nanoparticles, Springer, 2016.
[77] M. Wang, J. Wu, S. Yang, M. Knezevic, Z. Huang, Y. Zhao, T. Liu, B. Shen, J. Wang, Processing of an as-cast Al-7.5 wt%Y eutectic alloy by rolling and annealing to improve the tradeoff between strength and electrical conductivity, Mater. Sci. Eng. A, 890 (2024) 145950.
[78] J. Wang, G. Zhu, L. Wang, X. Zhang, M. Knezevic, X. Zeng, Strengthening mechanisms, hardening/softening behavior, and microstructure evolution in an LPSO magnesium alloy at elevated temperatures, Mater. Charact., 203 (2023) 113066.
[79] M. Wang, M. Knezevic, M. Chen, J. Li, T. Liu, G. Wang, Y. Zhao, M. Wang, Q. Liu, Z. Huang, D. Du, H. Gao, J. Wang, B. Sun, Microstructure design to achieve optimal strength, thermal stability, and electrical conductivity of Al-7.5wt.%Y alloy, Mater. Sci. Eng. A, 852 (2022) 143700.
[80] M. Wang, M. Knezevic, H. Gao, J. Wang, M. Kang, B. Sun, Phase interface induced stacking faults in Al-7.5Y alloy revealed by in-situ synchrotron X-ray diffraction and ex-situ electron microscopy, Mater. Charact., 179 (2021) 111322.
[81] K. Tao, F.C. Li, Y.H. Liu, E. Pineda, K.K. Song, J.C. Qiao, Unraveling the microstructural heterogeneity and plasticity of Zr50Cu40Al10 bulk metallic glass by nanoindentation, Int. J. Plast., 154 (2022) 103305.
[82] H. Wang, A. Dhiman, H.E. Ostergaard, Y. Zhang, T. Siegmund, J.J. Kruzic, V. Tomar, Nanoindentation based properties of Inconel 718 at elevated temperatures: A comparison of conventional versus additively manufactured samples, Int. J. Plast., 120 (2019) 380-394.
[83] M. Zecevic, Y.P. Korkolis, T. Kuwabara, M. Knezevic, Dual-phase steel sheets under cyclic tension–compression to large strains: Experiments and crystal plasticity modeling, J. Mech. Phys. Solids, 96 (2016) 65-87.
[84] A. Eghtesad, M. Knezevic, High-performance full-field crystal plasticity with dislocation-based hardening and slip system back-stress laws: Application to modeling deformation of dual-phase steels, J. Mech. Phys. Solids, 134 (2020) 103750.
[85] A. Eghtesad, M. Knezevic, A full-field crystal plasticity model including the effects of precipitates: Application to monotonic, load reversal, and low-cycle fatigue behavior of Inconel 718, Mater. Sci. Eng. A, 803 (2021) 140478.
[86] A. Eghtesad, K. Germaschewski, R.A. Lebensohn, M. Knezevic, A multi-GPU implementation of a full-field crystal plasticity solver for efficient modeling of high-resolution microstructures, Computer Physics Communications, 254 (2020) 107231.
[87] A. Eghtesad, T.J. Barrett, K. Germaschewski, R.A. Lebensohn, R.J. McCabe, M. Knezevic, OpenMP and MPI implementations of an elasto-viscoplastic fast Fourier transform-based micromechanical solver for fast crystal plasticity modeling, Advances in Engineering Software, 126 (2018) 46-60.

[88] A.M. Cantara, M. Zecevic, A. Eghtesad, C.M. Poulin, M. Knezevic, Predicting elastic anisotropy of dual-phase steels based on crystal mechanics and microstructure, International Journal of Mechanical Sciences, 151 (2019) 639-649.
[89] S. Daroju, T. Kuwabara, M. Knezevic, Experimental characterization and crystal plasticity modeling of dual-phase steels subjected to strain path reversals, Mechanics of Materials, 168 (2022) 104293.
[90] M. Zecevic, M.V. Upadhyay, E. Polatidis, T. Panzner, H. Van Swygenhoven, M. Knezevic, A crystallographic extension to the Olson-Cohen model for predicting strain path dependence of martensitic transformation, Acta. Mater., 166 (2019) 386-401.
[91] Z. Feng, E.M. Mamros, J. Ha, B.L. Kinsey, M. Knezevic, Modeling of plasticity-induced martensitic transformation to achieve hierarchical, heterogeneous, and tailored microstructures in stainless steels, CIRP Journal of Manufacturing Science and Technology, 33 (2021) 389-397.
[92] Z. Feng, S.-Y. Yoon, J.-H. Choi, T.J. Barrett, M. Zecevic, F. Barlat, M. Knezevic, A comparative study between elasto-plastic self-consistent crystal plasticity and anisotropic yield function with distortional hardening formulations for sheet metal forming, Mechanics of Materials, 148 (2020) 103422.
[93] K. Veasna, Z. Feng, Q. Zhang, M. Knezevic, Machine learning-based multi-objective optimization for efficient identification of crystal plasticity model parameters, Computer Methods in Applied Mechanics and Engineering, 403 (2023) 115740.
[94] D.J. Savage, Z. Feng, M. Knezevic, Identification of crystal plasticity model parameters by multi-objective optimization integrating microstructural evolution and mechanical data, Computer Methods in Applied Mechanics and Engineering, 379 (2021) 113747.
[95] T.J. Barrett, M. Knezevic, Modeling material behavior during continuous bending under tension for inferring the post-necking strain hardening response of ductile sheet metals: Application to DP 780 steel, International Journal of Mechanical Sciences, 174 (2020) 105508.